Supplementary Information for: Decentralized mechanical metawheelbot enabled by adaptive dynamic adhesion

Haofeng Liang,[1,*] Yu Sun,[1,†] Chenjie Wang,[1] Yafei Zhang,[2,‡] Laihao Yang,[1,§] and Xuefeng Chen[1]

[1] *School of Mechanical Engineering, Xi'an Jiaotong University, Xi'an, 710049, China*
[2] *Racah Institute of Physics, The Hebrew University of Jerusalem, Jerusalem, Israel*

CONTENTS

* H. Liang and Y. Sun contributed equally to this work.
† yu.sun@xjtu.edu.cn
‡ yafei.zhang@mail.huji.ac.il
§ yanglaihao@xjtu.edu.cn

SUPPLEMENTARY INFORMATION

I. THE ARCHITECTURE OF METAWHEEL

A. Asymmetric soft foot

The soft foot is the functional core of the metawheel, fabricated from PDMS to achieve the necessary compliance for interfacial adaptation (fig. S1). The asymmetry of the metawheel is derived from the specific orientation of the foot pads relative to the circumferential direction (fig. S2). This directional geometry creates a significant offset between the contact point and the wheel's center of rotation during rolling, which is essential for the dynamic diode adhesion effect. The low elastic modulus (experimentally characterized range: $0.15 \sim 0.42$ MPa) allows the feet to undergo significant elastic deformation without generating excessive internal stress[1, 2]. This characteristic is critical for two reasons: first, it lowers the energetic cost of deformation, ensuring that the gravitational potential energy is sufficient to drive the peeling process; second, it facilitates a gradual peeling of the trailing foot rather than an abrupt detachment, maintaining the stability required for self-holding adhesion on inverted surfaces.

The kinematics of the rolling stride are defined by the metawheel's periodicity. We define the stride angle α as the rotation angle required to transition the contact state from one foot to the next. For a metawheel with N foot pads distributed over a full circle (2π), the stride angle is geometrically defined as $\alpha = 2\pi/N$. The rotation through angle α constitutes a single stride, inducing elastic deformation that accumulates the critical strain energy barrier U_e^c. The rolling radius R is defined as the distance from the hub center to the tip of the foot pad. While the foot inclination angle β significantly influences the interfacial stress distribution and the critical strain energy, it does not alter the geometric stride angle α. Unless otherwise specified, two primary configurations were adopted in this study: a standard metawheel ($N = 20$, $\beta = 30°$) employed for robotic integration, anisotropy demonstrations, and characterizing the influence of angle β; and a miniaturized variant ($N = 12$, $\beta = 45°$) utilized specifically for the energy competition analysis, as detailed in Table S1 and fig. S2.

B. Rigid hub

The rigid hub is designed with an N-sided polygonal profile, fabricated via 3D printing with a layer height of 0.4 mm. By utilizing a dual-layer perimeter strategy, we achieved a structural thickness of merely 0.8 mm. This ultra-lightweight construction ensures structural integrity while minimizing the wheel's tare weight, thereby expanding the dynamic range for investigating payload-dependent rolling behaviors. Additionally, the polygonal internal geometry serves as a mechanical interface for internal loading; it constrains the rotational degree of freedom of the payload to prevent slippage, ensuring high stability for both variable-weight experiments and robotic integration.

C. Assembly of metawheel

The discrete configuration of the feet functions analogously to kirigami-enhanced adhesion mechanisms. Just as cuts in kirigami films introduce geometric discontinuities to arrest crack propagation, the physical gaps between the soft feet decouple the deformation fields of adjacent units[3, 4]. This stress detuning ensures that the stress concentration associated with the peeling of the trailing foot is not transmitted to the neighboring leading foot. By preventing the peeling front from propagating continuously across the interface, this isolation significantly enhances the overall robustness of the adhesion state.

Moreover, this discrete configuration endows the metawheel with intrinsic geometric adaptability. Analogous to the hierarchical discrete cilia of the gecko, which facilitate conformal contact on rough surfaces, the segmented architecture allows individual feet to accommodate local terrain variations independently[5]. This structural compliance ensures that the metawheel maintains effective interfacial contact even on complex substrates, enhancing adhesion reliability[6].

II. DESIGN OF ROBOTS

A. The wall-climbing robot

The wall-climbing robot functions as an integrated system powered by an onboard lithium-polymer battery and actuated by a DC motor. The structural chassis was fabricated via 3D printing, incorporating precision bearings

to enable smooth rotation. An infrared remote control module manages directional input, while the metawheel serves as the primary locomotive actuator (fig. S3). Notably, the control architecture is minimalist, providing only bidirectional torque output without active gait planning or closed-loop speed regulation; the climbing dynamics rely entirely on the intrinsic mechanical properties of the metawheel. The single-motor configuration inherently introduces a torque asymmetry relative to the non-driven side. To mitigate potential structural twisting or trajectory deviation resulting from this unilateral drive, we reinforced the chassis rigidity using additional fastening screws and a dedicated connecting bracket. This structural enhancement ensures that the robot maintains a stable heading without significant lateral deviation during locomotion. A detailed bill of materials and component specifications is provided in Table S2.

B. The adhesion-seeking metawheelbot

The adhesion-seeking metawheelbot is constructed by modular combining two independent wall-climbing units (fig. S4). The reconfiguration process involves removing the connecting brackets and follower rods from the original single-unit architecture. The pin, originally employed to secure the follower rods, are repurposed to articulate the connection between the two robotic units. Crucially, this pin connection is designed to retain a rotational degree of freedom between the coupled chassis. This mechanical compliance serves as a passive suspension, preventing kinematic locking and ensuring that the dual-wheel assembly maintains the flexibility required to accommodate minor terrain irregularities without structural binding.

The "adhesion-seeking" capability is an emergent behavior driven by the symmetry breaking of the wheel-substrate interaction dynamics. This configuration exploits the velocity differential induced by interfacial adhesion. When one metawheel encounters an adhesive zone, the transmission system must overcome the additional work of adhesion required to peel the soft feet. This increased torque significantly reduces the effective angular speed of the wheel on the adhesive side. Conversely, the metawheel on the non-adhesive substrate experiences minimal resistance, maintaining a higher rotational speed driven by the motor. This instantaneous speed differential generates a kinematic turning moment centered on the slower, adhering wheel. Consequently, the robot spontaneously steers towards the region of higher adhesion, effectively "seeking" onto the adhesive path without active electronic control. Detailed component specifications are provided in Table S2.

C. The adhesion-avoiding metawheelbot

The locomotion of the dual-wheel robot is driven by the relative rotation between the central double-wheel bracket and the metawheel assembly (fig. S5). A cross-axis transmission system, utilizing a pair of bevel gears, converts the motor's output torque into the relative motion of the connecting shaft, which is rigidly bound to the rotational degree of freedom of the metawheels, and the double-wheel bracket. To ensure that this internal torque generates effective wheel rotation rather than inducing the rotation of the bracket itself (chassis tumbling), the length of the bracket is sufficiently extended. This geometric design allows the bracket to act as a stable reaction lever against the substrate, constraining its rotation and forcing the metawheels to drive the system forward. The power supply and control architecture are identical to those of the wall-climbing robot, with detailed component specifications provided in Table S2.

The "adhesion-avoiding" behavior emerges from a symmetry-breaking instability triggered by differential interfacial conditions. The mechanism relies on the interplay between the central bracket's reaction torque and the adhesive state of the wheels. When one metawheel encounters a local adhesion zone while the other remains on a non-adhesive surface, the reaction force from the bracket tends to lift the chassis. The side with established adhesion remains anchored to the substrate due to the self-holding mechanism, whereas the non-adhesive side detaches and lifts off, creating a suspension effect. Consequently, the motor's drive is channeled exclusively into the rotation of the anchored metawheel. Since the bracket is positioned centrally along the connecting shaft rather than at the wheel axis, this unilateral anchoring shifts the instantaneous center of rotation, generating a significant yaw moment. This mechanical asymmetry forces the robot to veer away from its original heading, effectively steering it away from the high-adhesion region.

III. ENERGY CALCULATION

A. Assumption of energy balance

Across diverse configurations, the centroid speed of the metawheel consistently converges to a steady-state constant, albeit accompanied by minor periodic fluctuations. Furthermore, locomotion in the positive mode is characterized by strict, continuous rolling behavior (fig. S8). Based on these kinematic observations, we establish two fundamental assumptions to model the system's dynamics: (i) the rolling motion of the metawheel is a strictly periodic process, and (ii) the system maintains a macroscopic energy balance throughout this process. Consequently, the dynamic equilibrium dictates that the energy input must sustain both the periodic energy fluctuations and the continuous energy dissipation. The energetic components involved in this locomotion are mathematically synthesized as:

$$\Delta E_{\mathrm{p}} \rightleftharpoons U_{\mathrm{k}} + U_{\mathrm{e}} + U_{\mathrm{int}} + C_i v^{\alpha} \tag{1}$$

In this governing framework, the variation in gravitational potential energy over a single stride, ΔE_{p}, serves as the sole energy input. This input must be dynamically sufficient to sustain the fluctuating kinetic energy U_{k} of the system while overcoming the elastic strain energy U_{e} periodically accumulated in the deforming soft feet. Simultaneously, it must compensate for two continuous energy consumption mechanisms: the quasi-static interfacial energy required for successive peeling U_{int} and the rate-dependent dynamic dissipation $C_i v^{\alpha}$, where C_i represents the inherent structural damping coefficient and v denotes the steady-state rolling speed. Leveraging the assumption of periodicity, we sequentially formulate these energetic components to explicitly characterize the macroscopic locomotion dynamics.

B. Gravitational potential energy

To calculate the gravitational potential energy input, we first defined the total mass m of the metawheel, including any applied payloads. The effective rolling radius R is defined by the outer edge of the foot pad where the initial peeling occurs, as the continuous locus of these outer edges constitutes the rolling circle (fig. S2). When the metawheel rolls on an inclined surface, the decrease in gravitational potential energy over a single stride can be expressed as:

$$\Delta E_{\mathrm{p}} = mgR\frac{2\pi}{N}\sin\theta \tag{2}$$

where g is the gravitational acceleration (taken as 9.8 $\mathrm{m/s^2}$, N is the total number of soft feet, and θ is the inclination angle of the substrate, as defined in fig. S6.

C. Elastic potential energy

Given the periodic nature of the rolling process, the metawheel undergoes a continuous cycle of storing and releasing elastic strain energy. While the net change in strain energy over a complete single period is zero, this energy strictly governs the large deformation of the soft feet during the transition phase (fig. S12). Calculating the critical strain energy barrier $U_{\mathrm{e}}^{\mathrm{c}}$ required for the leading soft foot to establish a new adhesive contact is crucial for understanding the continuous rolling mechanism.

To accurately determine this barrier, we first characterized the elastic modulus E of the soft feet. Standard dumbbell-shaped tensile specimens and 90° peel samples were fabricated using the identical batch of PDMS utilized for the metawheel (figs. S9 to S11). The effective dimensions of the tensile specimens were defined as length l_{e}, width w_{e}, and thickness h_{e}. Assuming linear elasticity within this deformation range, the force-displacement data was processed using a custom computational script to extract the structural stiffness k_{e}. This enabled the calculation of the material's elastic modulus via:

$$E = \frac{k_{\mathrm{e}} l_{\mathrm{e}}}{w_{\mathrm{e}}} h_{\mathrm{e}} \tag{3}$$

This rigorously characterized elastic modulus was then incorporated into our finite element models. To quantify the critical strain energy barrier $U_{\mathrm{e}}^{\mathrm{c}}$, we established a computational model with the undeformed metawheel positioned on an inclined substrate as the initial condition. A gravitational load is applied to induce natural elastic deformation. Given that gravitational work alone may be insufficient to bridge the spatial gap for the next foot during

inverted rolling, a supplementary displacement boundary condition—directed along the gravity vector-is imposed at the metawheel's center of mass. This displacement forces the metawheel to deform until the subsequent leading foot establishes full, conformal contact. The total accumulated strain energy extracted at this geometric state defines the critical barrier $U_{\mathrm{e}}^{\mathrm{c}}$ (fig. S13).

D. Dissipation energy

To quantify the quasi-static interfacial energy dissipation U_{int}, we determined the energy release rate G_{c} of the PDMS-substrate interface. Standard 90° peel tests were conducted on adhesive specimens with a defined width of w_{ad}. By extracting the steady-state average peeling force $\bar{F}_{\mathrm{ad}}$ from the force-displacement curves, G_{c} is calculated as:

$$G_{\mathrm{c}} = \frac{\bar{F}_{\mathrm{ad}}}{w_{\mathrm{ad}}} \tag{4}$$

During continuous rolling, each soft foot establishes and breaks contact sequentially. The total quasi-static interfacial energy dissipated per stride is thus formulated as:

$$U_{\mathrm{int}} = G_{\mathrm{c}} h l \tag{5}$$

where l denotes the effective contact length along the rolling direction, and h represents the lateral width of the soft foot.

While U_{k} and U_{e} fluctuate significantly within a single rolling step, our assumption of steady-state periodicity ensures that their net variations over a complete, full stride are exactly zero. Consequently, the dynamic equilibrium dictates that the net gravitational potential energy input over a stride is exclusively balanced by the quasi-static interfacial peeling and the rate-dependent dynamic damping. By synthesizing this periodic boundary condition with Eqs. S1 and S5, the dynamic dissipation term can be explicitly decoupled and isolated:

$$C_i v^{\alpha} = \Delta E_{\mathrm{p}} - U_{\mathrm{int}} \tag{6}$$

This simplified formulation allows us to directly quantify the complex dynamic viscoelastic losses and structural damping using purely macroscopic, experimentally accessible parameters.

E. Peeling assumptions

To simulate the interfacial debonding between the material adhesion and the substrate via finite element analysis, we implemented a cohesive zone model governed by a bilinear traction-separation law (fig. S14). To prevent non-physical interpenetration while ensuring optimal numerical convergence, the reversible, initial linear elastic behavior of the interface was governed by the solver's default penalty stiffness. Damage initiation is predicted using a quadratic nominal stress criterion, formulated as:

$$\left(\frac{\sigma_{\mathrm{n}}}{\sigma_{\max}}\right)^2 + \left(\frac{\sigma_{\mathrm{t}}}{\sigma_{\max}}\right)^2 + \left(\frac{\sigma_{\mathrm{s}}}{\sigma_{\max}}\right)^2 = 1 \tag{7}$$

where σ_{n}, σ_{t}, and σ_{s} denote the contact traction in the normal and two orthogonal shear directions, respectively, and $\sigma_{\max}$ is the specified interfacial strength. To ensure mesh objectivity and numerical robustness during the delamination process, the damage evolution is dictated by an energy-based formulation with linear softening. The energetic threshold for complete separation is defined by the critical fracture energy (or adhesion energy), G_{c}, which represents the work required to separate a unit area of the interface. This energy-based evolution intrinsically defines the maximum interfacial separation at failure, δ_{f}, through the mathematical relation $G_{\mathrm{c}} = \frac{1}{2}\sigma_{\max}\delta_{\mathrm{f}}$. The interface is considered completely delaminated when the dissipated energy reaches G_{c}, at which point the load-bearing capacity reduces to zero. In our simulations, we assumed isotropic cohesive properties across all normal and tangential directions.

IV. ADDITIONAL DEMONSTRATIONS

The purely mechanical geometric adaptability of the metawheel is comprehensively showcased in Movie S1, which includes dynamic interactions with sharp corners and curved surfaces. Furthermore, explicit two-dimensional dynamic

simulations for configurations with $\beta = 30°$ and $\beta = 90°$ are also provided in Movie S1. To systematically demonstrate the dynamic diode adhesion of the metawheel, we first rigorously defined its positive and negative modes (fig. S7). The explicit simulation process of this behavior is captured in Movie S2 and detailed in fig. S15. We further expanded these demonstrations to include various metawheel configurations rolling on inclined surface in both positive and negative modes, confirming the universality of this anisotropic adhesion (fig. S16). Dictated by the energy barrier characteristics of the metawheel, this strong anisotropy can be attenuated by either increasing the system's mass or decreasing its elastic modulus, as illustrated in fig. S17 and Movie S2. Crucially, this tunable anisotropy can be directly applied to control the adhesive behavior of the wall-climbing robot: climbing function is inherently prohibited when operating in the negative mode (fig. S18, Movie S3). Ultimately, this anisotropic nature endows the robotic system with emergent potential for environmental interaction. It allows the robot to adapt its locomotion behavior by distinguishing between its own positive and negative modes, or to facilitate complex physical interactions with other active units (fig. S19, Movie S4).

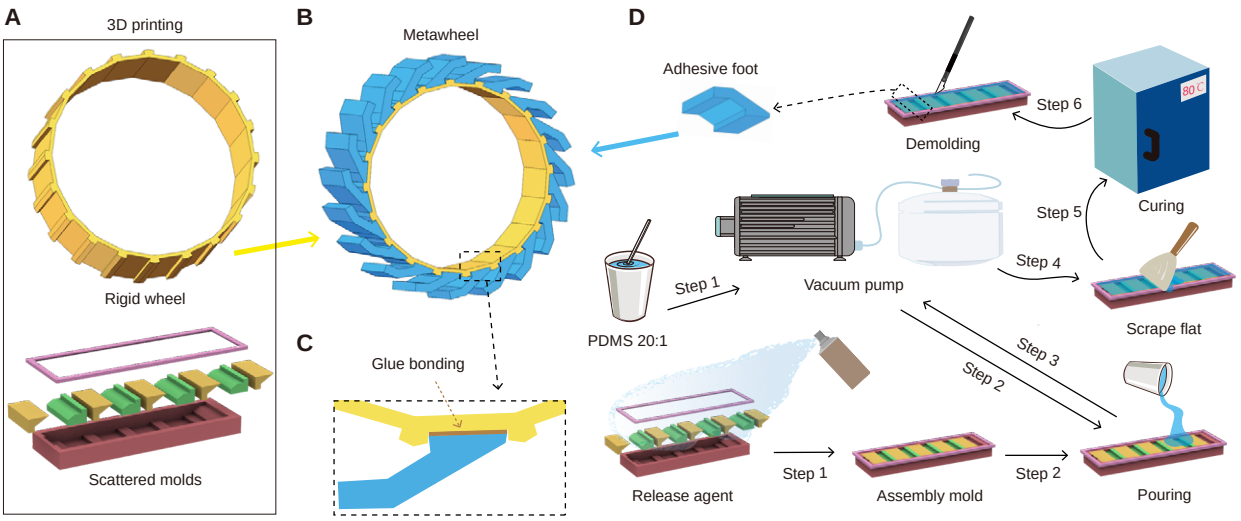

Supplementary Figure 1. **Manufacturing process of metawheels.** (**A**) Using 3D printing technology to manufacture wheel hubs and scattered molds for producing adhesive feet. (**B**) The metawheel consists of a wheel hub and adhesive feet. (**C**) The hub and adhesive feet are connected with glue. (**D**) Manufacturing process of adhesive feet. Step 1: Vacuum-treating the thoroughly mixed PDMS and crosslinking agent mixture, and assembling the scattered molds that have been sprayed with a release agent. Step 2: Pouring the PDMS into the assembled molds. Step 3: Vacuum-treating the molds containing PDMS. Step 4: Scraping the liquid surface to remove excess PDMS and level it. Step 5: Treating the molds in an 80°C constant temperature oven for one hour. Step 6: Demolding and removing impurities.

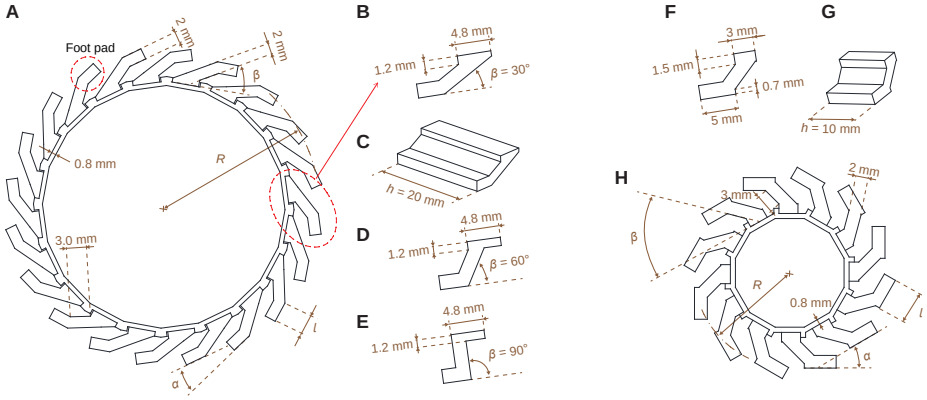

Supplementary Figure 2. **Geometric parameters and design configurations of the metawheel.** Specifications for the metawheel configuration featuring $N = 20$ soft feet: (**A**) Dimensional parameters, with the inset illustrating the assembly of 30° soft feet onto the rigid hub. (**B**, **D**, and **E**) Detailed geometric definitions of soft-foot angles $\beta = 30°$, 60°, and 90°, respectively. (**C**) Cross-sectional view depicting the wheel thickness of 20 mm. (**F**–**H**) Specifications for the metawheel configuration featuring $N = 12$ soft feet: (**F**) Geometric parameters of the 45° soft foot and its corresponding hub architecture. (**G**) Cross-sectional view showing the wheel thickness of 10 mm. (**H**) Dimensional parameters for the $N = 12$, where the inset clarifies the assembly method of the 45° foot. Across all configurations, l denotes the contact length, h represents the foot width, α signifies the characteristic rotation angle, and R indicates the rolling radius.

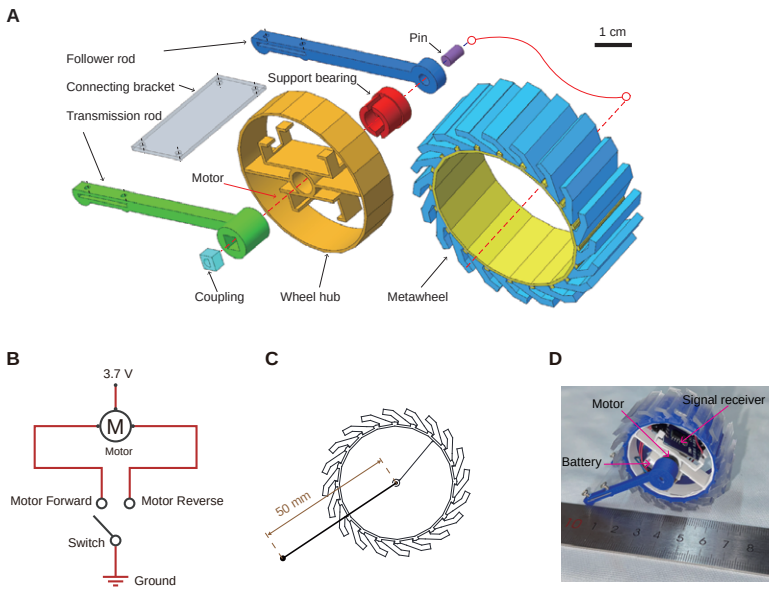

Supplementary Figure 3. **Design, fabrication, and control of the wall-climbing robot.** (**A**) Assembly and mechanical transmission of the robot. The metawheel is secured to the wheel hub via an interference fit, which is further integrated with the motor housing to constrain relative degrees of freedom. The motor shaft drives the transmission rod through a rigid coupling. A connection bracket bridges the transmission rod and the follower rod, ensuring synchronized movement. The follower rod is supported by a pin joint within a bearing mounted on the distal end of the motor, allowing load transmission without impeding rotation. Upon motor activation, the assembly generates relative rotation between the rods and the metawheel. (**B**) Remote control scheme. The robot is operated via an infrared remote, supporting three modes: forward, reverse, and stop. (**C**) Geometric configuration of the rods, featuring a characteristic length of 50 mm relative to the metawheel's center of rotation. (**D**) Photograph of the fabricated wall-climbing robot, showing the integration of the onboard battery, motor, and signal receiver. The overall chassis length is approximately 67 mm.

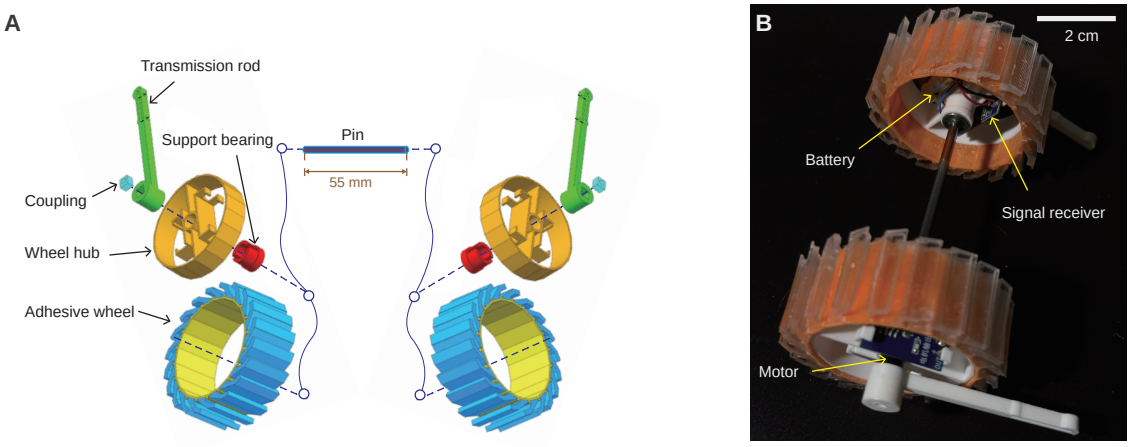

Supplementary Figure 4. **Design of the adhesion-seeking dual-wheel robot.** (**A**) Schematic of the modular reconfiguration for the adhesion-seeking metawheelbot. The assembly is derived from two single-wheel wall-climbing robot units. By removing one side of the follower rod from each unit and coupling them via a common shaft through the integrated bearings, a coordinated dual-wheel system is formed. (**B**) Photograph of the fabricated adhesion-seeking dual-wheel robot.

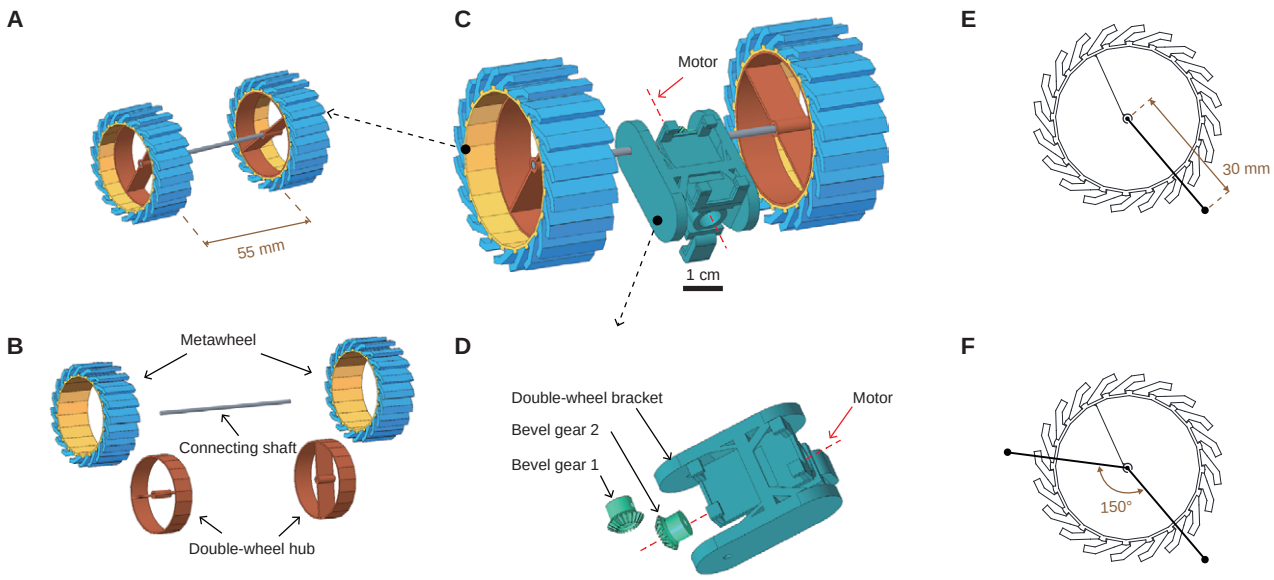

Supplementary Figure 5. **Design and mechanical transmission of the adhesion-avoiding metawheelbot.** (**A**) and (**B**) Standard dual-wheel configuration. Two metawheels are secured to a common shaft via a double-wheel hub using interference fits to prevent relative rotation. (**C**) Design of the adhesion-avoiding metawheelbot equipped with an integrated orthogonal transmission system. (**D**) Detailed view of the transmission assembly, which utilizes a pair of bevel gears supported by precision bearings. Two set screws are employed for fixation: one couples the motor output shaft to bevel gear 2, and the second secures bevel gear 1 to the main shaft. This configuration enables the motor to drive the relative rotation between the dual-wheel system and the double-wheel bracket, which is coupled to the motor via an interference fit. (**E**) Geometric parameters showing a 30 mm offset between the double-wheel bracket and the metawheel center of rotation. (**F**) Configuration of the bracket assembly, highlighting the 150° angle between the front and rear brackets as implemented in Fig.5E.

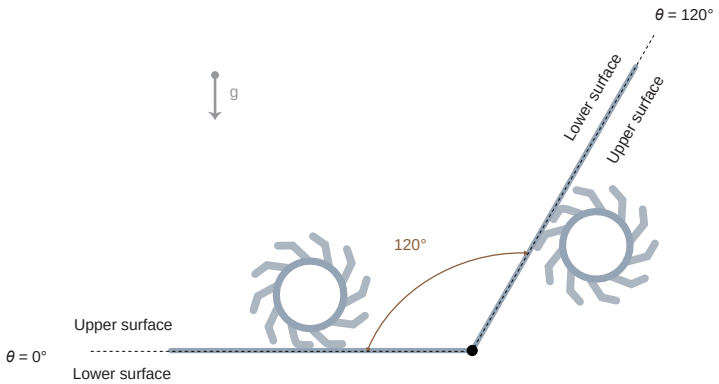

Supplementary Figure 6. **Definition of the inclination angle θ.** The angle θ is measured relative to the horizontal plane ($\theta = 0°$). The substrate rotates about a fixed pivot while the metawheel remains on its upper surface. A representative state at $\theta = 120°$ is illustrated.

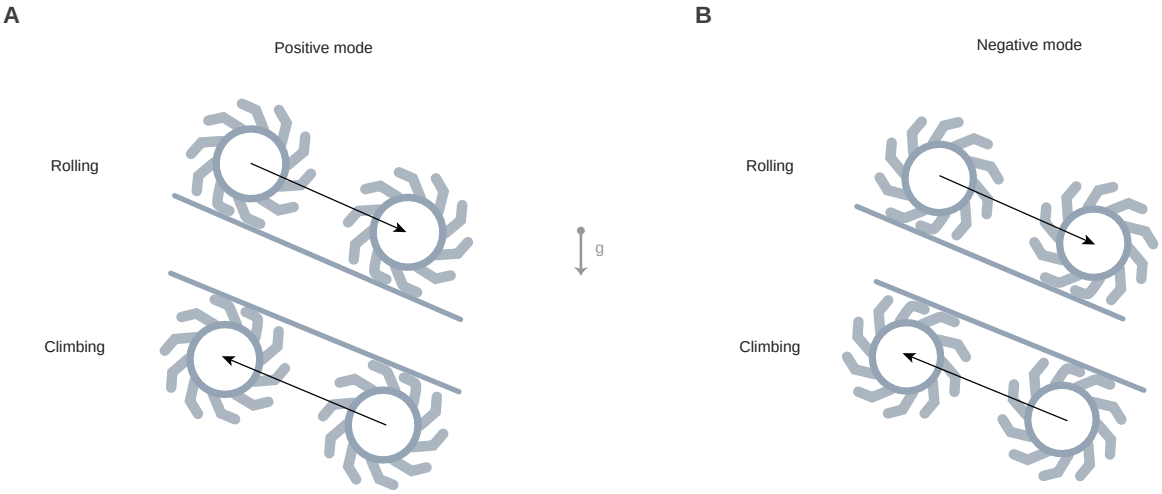

Supplementary Figure 7. **Locomotion modes of the metawheel.** (**A**) Definition of positive mode. Locomotion is classified as "rolling" when gravity performs positive work and "climbing" or "up-climbing" when gravity performs negative work. (**B**) Schematic of rolling and climbing behaviors within the negative mode.

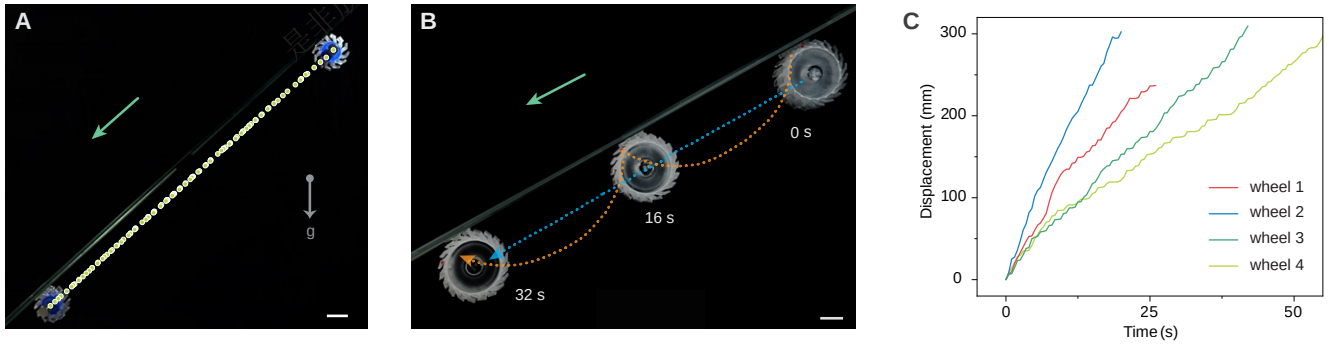

Supplementary Figure 8. **Self-holding adhesion and rolling kinematics of metawheels on inverted surfaces.** (**A**) Demonstration of the metawheel in positive mode achieving self-holding adhesion on an inverted surface. (**B**) Rolling-based locomotion pattern of the metawheel in positive mode. (**C**) Displacement-time profiles of different metawheel configurations exhibiting quasi-uniform rolling on an inverted surface. The configurations include: Wheel 1 (m = 35.8 g), Wheel 2 (m = 35.8 g), Wheel 3 (m = 35.4 g), and Wheel 4 (m = 35.4 g), all tested at an inclination angle of 135°; Source data are provided in Data 1. Scale bars: 2 cm.

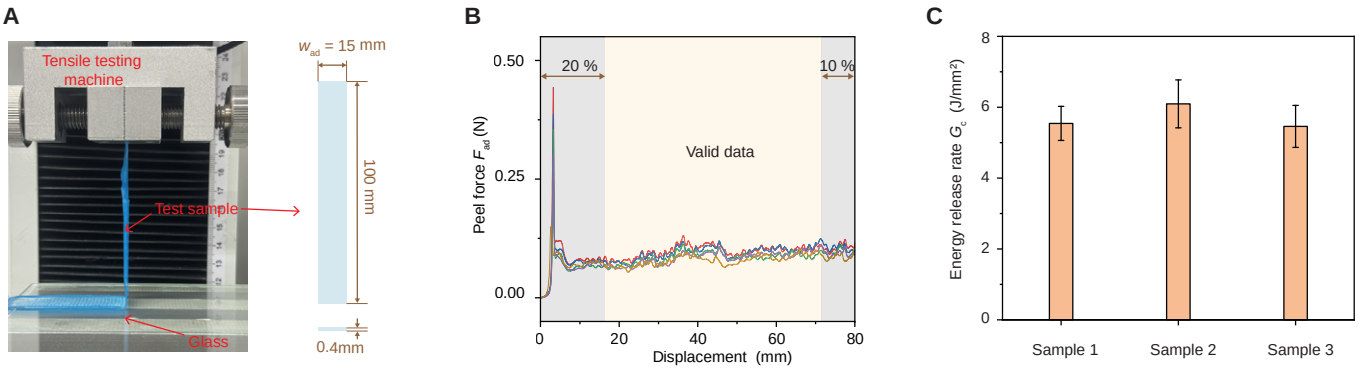

Supplementary Figure 9. **Characterization of energy release rate G_c.** (**A**) Setup for 90° peel tests on glass substrates using PDMS samples (100 × 15 (w_{ad}) ×0.4 mm) consistent with metawheel fabrication. (**B**) Representative peel force (F_{ad}) curve. The steady-state region (middle 70% of the 80 mm stroke) was used for analysis. (**C**) Average G_c and mean peeling force $\bar{F}_{ad}$ calculated from three specimens ($n = 5$) to define the interfacial mechanics of the metawheel.

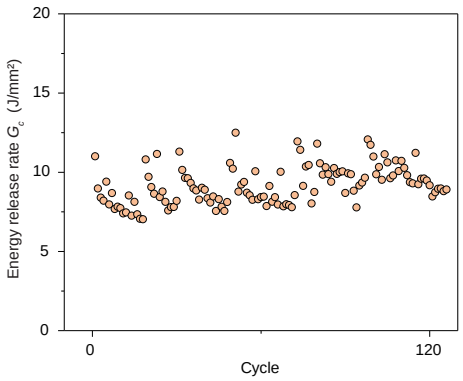

Supplementary Figure 10. **Interfacial durability.** Characterization of PDMS soft feet over 120 peeling cycles. The substrate was cleaned with anhydrous ethanol every 10 cycles to maintain surface consistency. The stable adhesion results confirm the material's robustness and the reproducibility of the metawheel's rolling behavior.

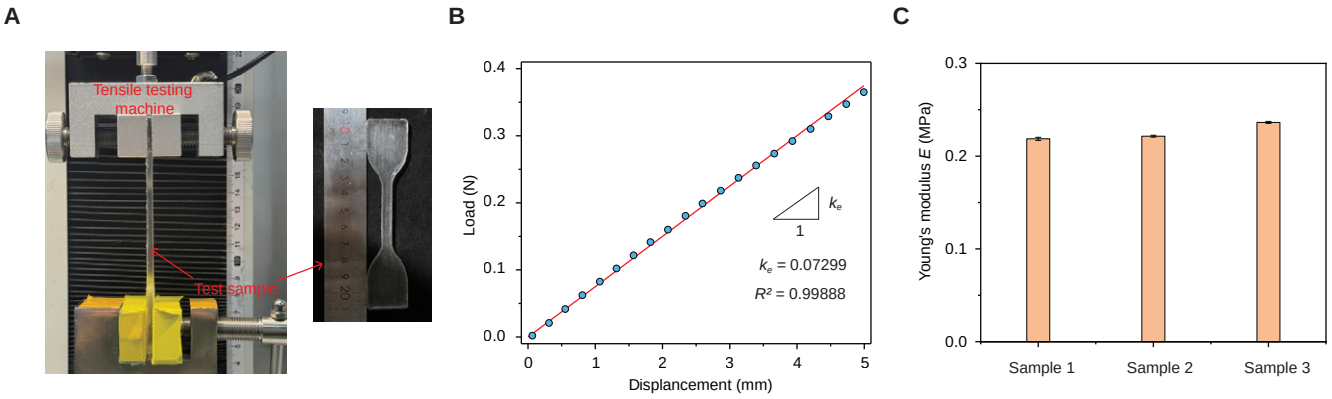

Supplementary Figure 11. **Characterization of elastic modulus** E**.** (**A**) Experimental setup for uniaxial tensile testing. PDMS specimens were fabricated from the same batch as the metawheel soft feet. The effective gauge dimensions are $l_e = 40$ mm (length), $w_e = 5.6$ mm (width), and $h_e = 2.4$ mm (thickness). During the uniaxial tensile testing, the maximum displacement was set to 5 mm. (**B**) Load-displacement curves obtained from the PT-1176 testing machine. The structural stiffness k_e was determined by the slope of the linear fitting. (**C**) The elastic modulus E was calculated by averaging results from three independent specimens ($n = 3$) to define the material properties.

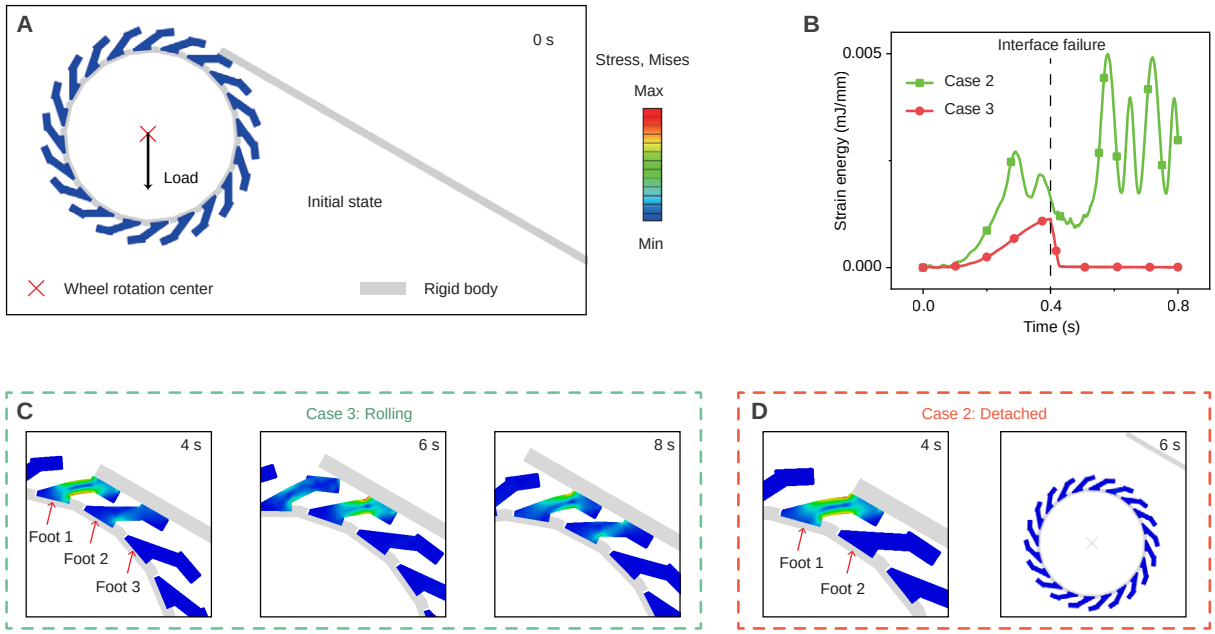

Supplementary Figure 12. **Load-dependent movement modes and energetic transitions in simulation.** (**A**) Simulation setup and initial state for explicit dynamic analysis. Geometric parameters are consistent with fig. S2A. The interfacial properties are defined by $G_c = 7.2$ J/m^2 and $\sigma_{max} = 0.028$ MPa. Analysis is conducted under center-of-mass loads in the absence of gravitational acceleration. (**B**) Strain energy evolution of the soft feet under heavy (0.0007 N/mm) and light (0.00035 N/mm) loads. The simulation comprises two stages ($0-4$ s and $4-8$ s); at $t = 4$ s, a boundary condition for initial interfacial failure is applied. (**C**) Continuous rolling process under heavy load. During $0-4$ s, foot 1 undergoes adaptive deformation to induce contact for foot 2. Following interfacial failure at 4 s, foot 1 peels off, while from $4-8$ s, foot 2 deforms to establish new contact for foot 3. (**D**) Detachment process under light load. Due to insufficient adaptive deformation, foot 2 fails to establish contact during the $0-4$ s interval, resulting in system detachment after the initial interfacial failure.

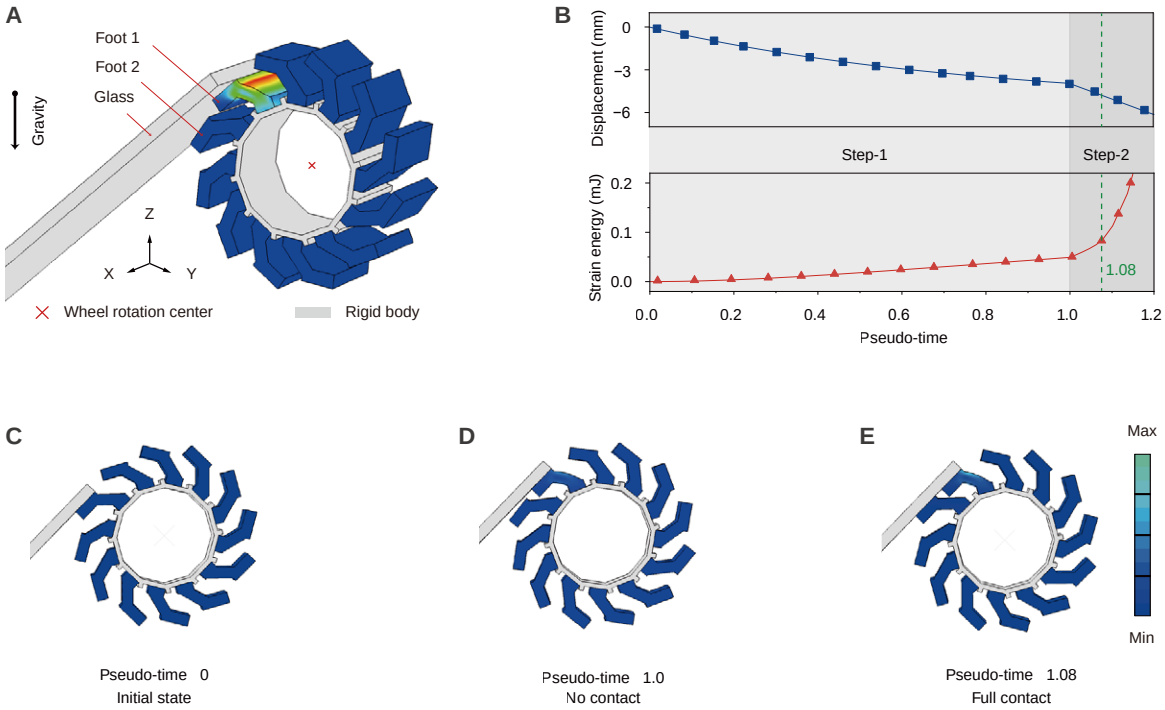

Supplementary Figure 13. **Calculation of the strain energy barrier U_e^c.** (**A**) Simulation setup and initial state for static analysis. Geometric parameters are consistent with fig. S2H. In Step 1, gravitational acceleration is applied along the -Z direction. In Step 2, a downward (-Z) displacement is applied to the center of mass while foot 1 remains bonded to the interface. (**B**) Relationship between displacement, soft-foot strain energy, and pseudo-time. (**C** to **E**) Representative configurations illustrating the transition to contact: initial state (**C**), gravity-loaded state where foot 2 remains out of contact with the glass surface (**D**), and the application of external displacement forcing foot 2 into full interfacial contact (**E**). The strain energy associated with this contact transition is defined as the barrier U_e^c.

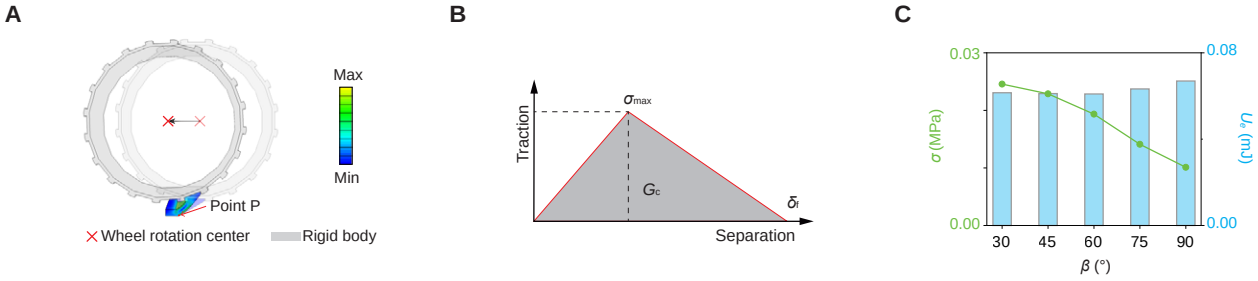

Supplementary Figure 14. **Peeling simulation of the metawheel.** (**A**) Simulation setup for the peeling process. Variations in strain energy and interfacial stress are modeled within a single stride. The soft foot is horizontally constrained while a displacement boundary condition of $2\pi R/N$ is applied to trigger the positive mode. The maximum stress at Point P serves as the output metric for characterizing peeling force. (**B**) Implementation of the quadratic traction-separation criterion as the governing law for the peeling simulation. (**C**) Interfacial stress and strain energy corresponding to different soft-foot angles β, recorded at the completion of one full stride.

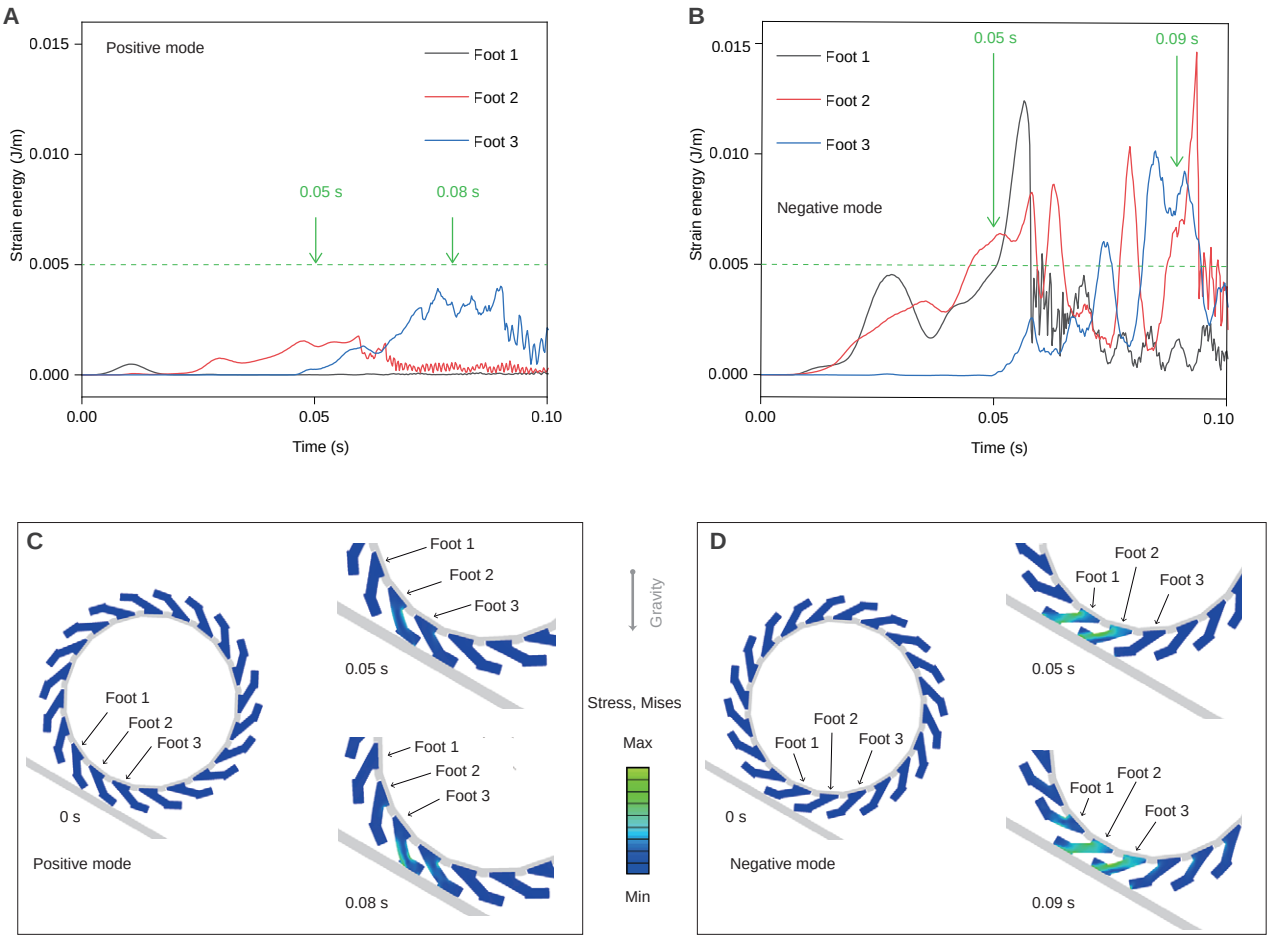

Supplementary Figure 15. **2D explicit simulation of metawheel dynamics on a 30° slope.** (**A**) Time-dependent strain energy in the positive mode, which maintains a consistently low energy level. (**B**) Time-dependent strain energy in the negative mode, characterized by significant energy peaks during interfacial contact. (**C**) Sequential snapshots of the positive mode at 0.05 s and 0.08 s, illustrating the establishment of contact strides. (**D**) Sequential snapshots of the negative mode at 0.05 s and 0.08 s showing the corresponding motion.

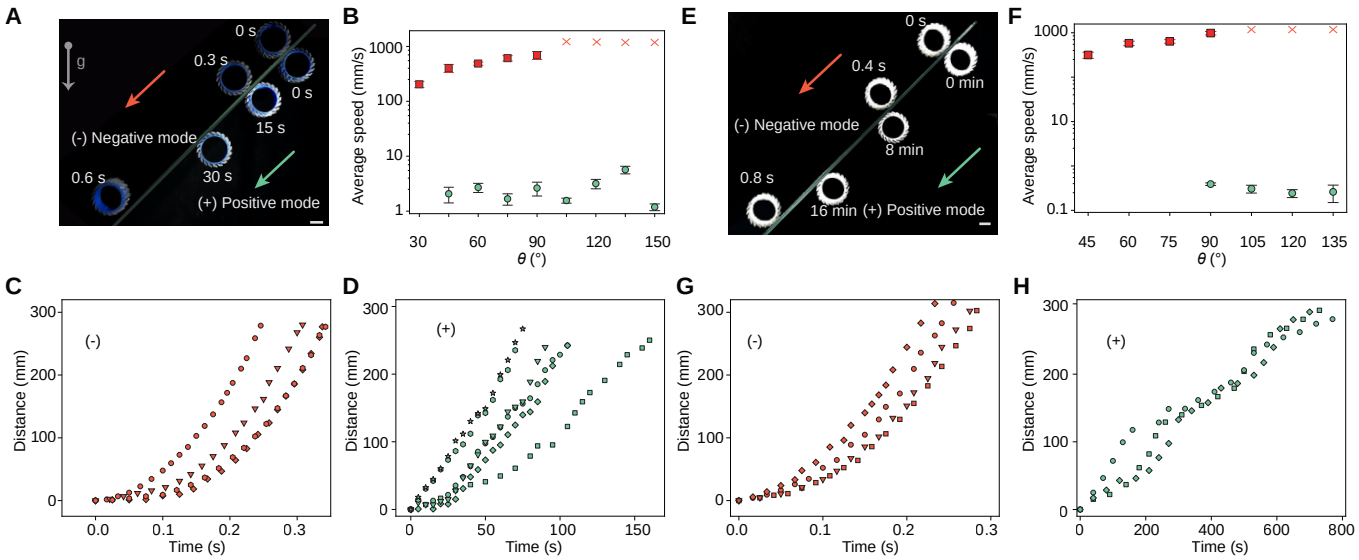

Supplementary Figure 16. **Universality of dynamic diode adhesion in different wheel configurations.** (**A**–**D**) First metawheel configuration (E = 0.29 MPa, G_c = 2.67 J/m^2): (**A**) snapshots illustrating the contrast between motion modes; (**B**) rolling speeds in positive (+) and negative (−) modes across $\theta \in [30°, 150°]$; (**C**, **D**) displacement-time curves at $\theta = 90°$ for negative and positive modes, respectively. (**E**–**H**) Second metawheel configuration (E = 0.25 MPa, G_c = 3.79 J/m^2) following the same sequence, demonstrating the consistent kinematic disparity and physical robustness of the direction-dependent adhesion mechanism. Scale bars: 2 cm.

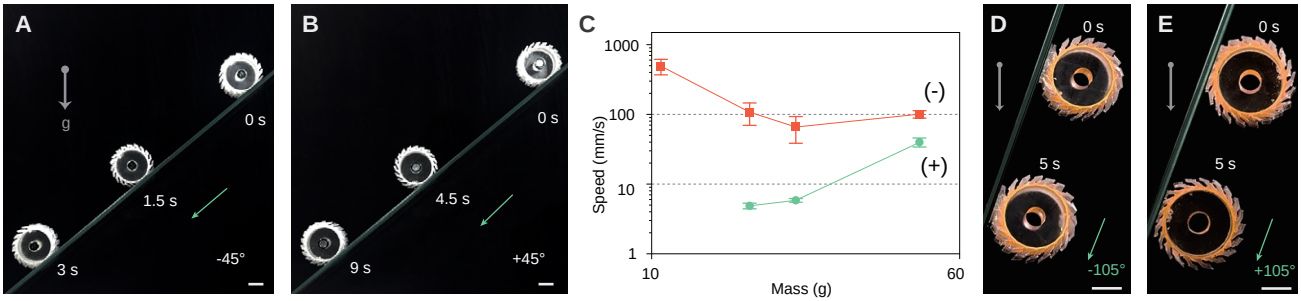

Supplementary Figure 17. **Attenuation of directional anisotropy in metawheel rolling.** (**A**) The addition of eccentric weights reduces the performance discrepancy between positive and negative modes. (**B**) Speed profiles of positive and negative modes as a function of total mass. The difference in rolling speeds diminishes as the mass increases ($E = 0.25$ MPa, $G_c = 3.79$ J/m^2). (**C**) Influence of the elastic modulus on rolling anisotropy. Reducing the modulus lowers the energy barrier, thereby minimizing the kinetic divergence between rolling directions ($E = 0.15$ MPa, $G_c = 7.4741$ J/m^2). Scale bars: 2 cm.

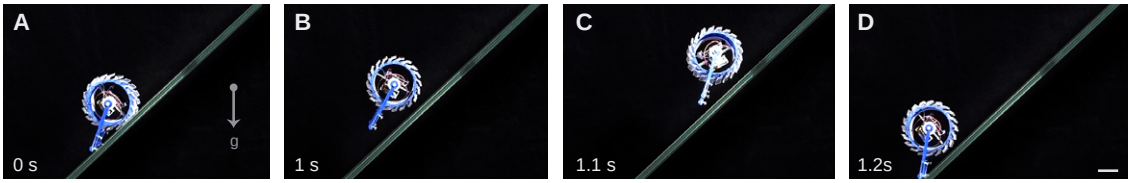

Supplementary Figure 18. **Climbing failure in the negative mode on a 45° slope.** (**A**) Initial stationary state of the robot on a slope (0 s). (**B** and **C**) Dynamic response at 1 s and 1.1 s. The high energy barrier inherent to the negative mode induces bouncing, which prevents the establishment of stable adhesion. (**D**) Detachment and subsequent fall from the slope at 1.2 s due to the failure to achieve interfacial adhesion. Scale bars: 2 cm.

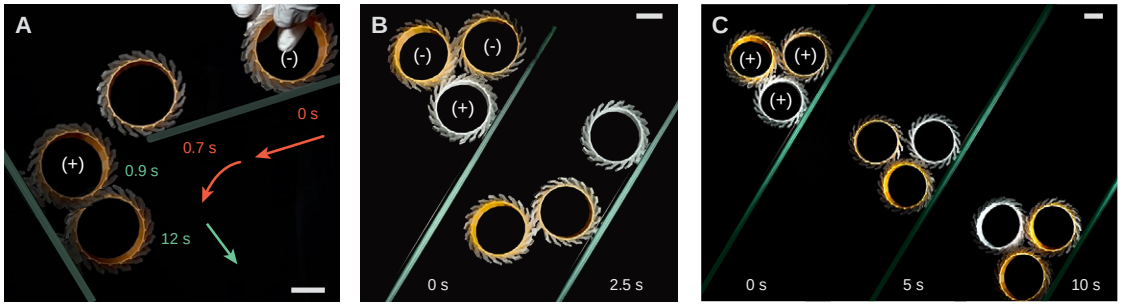

Supplementary Figure 19. **Emergent interaction behaviors enabled by the dynamic diode mechanism.** (**A**) A metawheel in negative mode rolls down a slope and lands on a secondary surface; the impact triggers a transition to the positive mode, thereby activating interfacial adhesion. (**B**) A pre-coupled pair of negative-mode metawheels is placed onto a positive-mode metawheel. The mismatch between modes prevents mutual coupling, leading to the detachment of the top pair. (**C**) Three metawheels operating in synchronous positive modes achieve mutual coupling, forming a collective assembly that moves as a single unit. Scale bars: 2 cm.

TABLE I. **Geometric and physical parameters of the primary metawheel configurations.** Two distinct configurations were characterized: a standard metawheel ($N = 20, \beta = 30°$) employed for robotic integration and anisotropy demonstrations, and a miniaturized variant ($N = 12, \beta = 45°$) utilized specifically for energy competition analysis. The parameters include rolling radius (R), bare wheel mass (m), soft-foot contact length (l) and lateral width (h), soft-foot angle (β), number of feet (N), and the geometric stride angle ($\alpha = 2\pi/N$).

R (mm)	m (g)	l (mm)	h (mm)	β (°)	N	α (°)
25.7	11.1±0.2	4	20	30	20	18
27.0	11.2	4	20	90	20	18
14.8	3.2	5	10	45	12	30

TABLE II. **Component specifications and bill of materials for robotic demonstrators.** The table details the commercial off-the-shelf (COTS) components used in each robotic platform. Bearing dimensions are denoted as inner diameter × outer diameter × width. The wall-climbing robot was characterized using two distinct voltage options. All custom structural chassis were fabricated via 3D printing. Components were mechanically fastened where possible, or secured using structural adhesive.

Robot Type	**Actuation (Motor)**	**Mechanical Components**	**Electronics & Power**
Wall-climbing robot	3 V, 60 rpm, 60 mA (×1) *or* 6 V, 149 rpm, 50 mA (×1)	Bearing, 2×5×2 mm (×1); Screws, M1.2×6 PA (×4)	IR Control Module (×1); Li-Po, 3.7 V, 60 mAh *or* Li-Po, 7.4 V, 100 mAh (×1)
Adhesion-seeking metawheelbot	3 V, 46 rpm, 60 mA (×2)	Bearing, 2×5×2 mm (×2); Steel Shaft, ϕ2 mm×55 mm (×1)	IR Control Module (×2); Li-Po Battery, 3.7 V, 60 mAh (×2)
Adhesion-avoiding metawheelbot	3 V, 46 rpm, 60 mA (×1)	Bearing, 2×5×2 mm (×2); Steel Shaft, ϕ2 mm×55 mm (×1); Bevel gears, 0.5 mod, 12-tooth (×2)	IR Control Module (×1); Li-Po Battery, 3.7 V, 60 mAh (×1)

Caption for Movie S1.

Metawheel achieves robust adhesive rolling in positive mode. [00:04] Cooperative motion of the metawheel and a gecko. [00:19] Mechanical metawheel rolling on an inverted surface. [00:40 Metawheel traversing surfaces with corners. [00:57] Metawheel traversing curved surfaces. [01:10] Effect of load on the adhesion state of the metawheel. [01:22] Rolling of the metawheel at different soft-foot angles.

Caption for Movie S2.

Dynamic diode adhesion drives the metawheel to perform asymmetric motion. [00:04] The motion of the metawheel on different slopes in positive and negative modes. [00:15] Asymmetric motion of the metawheel in the valley-crossing maneuver. [00:24] Metawheel transition from negative mode to positive mode. [00:30] Metawheel transition from positive mode to negative mode. [00:39] Finite element method simulation of the metawheel in positive and negative modes. [00:53] Weakening the anisotropy of the metawheel's motion by increasing the load and decreasing the elastic modulus.

Caption for Movie S3.

Driving the metawheel to achieve wall-climbing motion. [00:04] A metal stick driving the metawheel to perform wall-climbing motion. [00:15] Another metawheel driving the metawheel to perform wall-climbing motion. [00:24] The metawheel wall-climbing robot traversing an orthogonal circuit. [00:30] Metawheel transition from positive mode to negative mode. [00:40] The metawheel wall-climbing robot traversing a curved circuit. [00:57] The metawheel wall-climbing robot traversing a kink path. [01:02] High-load and high-speed motion of the metawheel wall-climbing robot. [01:05] Controlling the adhesion and detachment of the metawheel wall-climbing robot via mode transitions.

Caption for Movie S4.

Locomotion of dual-metawheel systems. [00:04] Coupling of two positive-mode metawheels in series. [00:15] Inability to couple a positive-mode and a negative-mode metawheel in series. [00:24] A positive-mode and a negative-mode metawheel initiate a turn in a parallel configuration. [00:33] Two positive-mode metawheels in a parallel configuration avoid wet areas and rough sites. [00:45] Motor-driven metawheelbot tend to move toward smooth surfaces without central control. [00:55] Interface-guided metawheelbot complete a multi-target retrieval task. [01:04] Controlling environmental interaction via the rotational direction of the metawheelbot.

Caption for Data S1.

Geometric specifications, energetic parameters, and kinematic performance of Metawheel prototypes (Wheels 1–8). This dataset tabulates the structural parameters (mass m, foot angle β, radius R, contact length l, and foot width h), inclination angles (θ), and the corresponding energy distribution per stride (gravitational potential ΔE_{p}, critical strain energy $U_{\mathrm{e}}^{\mathrm{c}}$, interfacial dissipation U_{int}) and the system damping coefficient (C_i). These parameters, derived from experiments and FEA simulations presented in Fig. 2F and H, elucidate the phase transitions (Stationary, Detachment, Unstable, Rolling) and steady-state speeds (v) governed by the competition between gravitational work and adhesive-elastic barriers.

[1] Xia, S., Ponson, L., Ravichandran, G. & Bhattacharya, K. Toughening and asymmetry in peeling of heterogeneous adhesives. *Phys. Rev. Lett.* **108**, 196101 (2012).

[2] Bartlett, M. D., Case, S. W., Kinloch, A. J. & Dillard, D. A. Peel tests for quantifying adhesion and toughness: A review. *Progress in Materials Science* **137**, 101086 (2023).

[3] Hwang, D.-G., Trent, K. & Bartlett, M. D. Kirigami-inspired structures for smart adhesion. *ACS Appl. Mater. Interfaces* **10**, 6747–6754 (2018).

[4] Zhu, H. *et al.* Mechanics of regulatable hydrogel adhesion with elastic heterogeneity. *Journal of the Mechanics and Physics of Solids* **175**, 105304 (2023).

[5] Tian, Y. *et al.* Adhesion and friction in gecko toe attachment and detachment. *Proceedings of the National Academy of Sciences* **103**, 19320–19325 (2006).

[6] Rao, Z. *et al.* Curvy, shape-adaptive imagers based on printed optoelectronic pixels with a kirigami design. *Nat Electron* **4**, 513–521 (2021).